Philosophical Magazine
Publication details, including instructions for authors and subscription information:
http://www.tandfonline.com/loi/tphm20

Transmission electron microscopy study of phase compatibility in low hysteresis shape memory alloys

Rémi Delville [a], Sakthivel Kasinathan [b], Zhiyong Zhang [b], Jan Van Humbeeck [c], Richard D. James [b] & Dominique Schryvers [a]

[a] Electron Microscopy for Materials Science (EMAT), University of Antwerp, Groenenborgerlaan 171, B-2020, Antwerp, Belgium

[b] Department of Aerospace Engineering and Mechanics, University of Minnesota, Minneapolis, Minnesota 55455, USA

[c] Department MTM, Catholic University of Leuven, de Croylaan 2, B-3001, Heverlee, Belgium

Published online: 15 Jan 2010.

To cite this article: Rémi Delville, Sakthivel Kasinathan, Zhiyong Zhang, Jan Van Humbeeck, Richard D. James & Dominique Schryvers (2010) Transmission electron microscopy study of phase compatibility in low hysteresis shape memory alloys, Philosophical Magazine, 90:1-4, 177-195, DOI: 10.1080/14786430903074755

To link to this article: http://dx.doi.org/10.1080/14786430903074755

Philosophical Magazine
Vol. 90, Nos. 1–4, 7–28 January 2010, 177–195

Taylor & Francis
Taylor & Francis Group

Transmission electron microscopy study of phase compatibility in low hysteresis shape memory alloys

Rémi Delville[a]*, Sakthivel Kasinathan[b], Zhiyong Zhang[b], Jan Van Humbeeck[c], Richard D. James[b] and Dominique Schryvers[a]

[a]*Electron Microscopy for Materials Science (EMAT), University of Antwerp, Groenenborgerlaan 171, B-2020, Antwerp, Belgium;* [b]*Department of Aerospace Engineering and Mechanics, University of Minnesota, Minneapolis, Minnesota 55455, USA;* [c]*Department MTM, Catholic University of Leuven, de Croylaan 2, B-3001, Heverlee, Belgium*

(*Received 15 November 2008; final version received 25 May 2009*)

Recent findings have linked low hysteresis in shape memory alloys with phase compatibility between austenite and martensite. To investigate the evolution of microstructure as phase compatibility increases and hysteresis is reduced, transmission electron microscopy was used to study the alloy system $Ti_{50}Ni_{50-x}Pd_x$, where the composition is systemically tuned to approach perfect compatibility. Changes in morphology, twinning density and twinning modes are reported, along with special microstructures occurring when compatibility is achieved. In addition, the interface between austenite and a single variant of martensite was studied by high-resolution and conventional electron microscopy. The low energy configuration of the interface detailed in this article suggests that it plays an important role in the lowering of hysteresis compared to classical habit plane interfaces.

Keywords: electron microscopy; martensitic transformation; interfaces; hysteresis

1. Introduction

Hysteresis in shape memory alloys (SMA) plays an important role in their thermo-mechanical behavior with important technological consequences in the design and operation of these materials. Hysteresis is the macroscopic manifestation of the energy dissipated during a phase transformation. One mechanism of dissipation is the creation of defects that accumulate during cycling to eventually become the sites of crack initiation [1]. In such cases, hysteresis also correlates with fatigue, an important parameter for applications, especially for systems subjected to cyclic loading. The sources of hysteresis and their relative importance are not yet fully understood due to their actions at different spatial scales [2] and their possible interdependence. At the microscopic scale, both the nucleation of the new phase and the interactions of interfaces with defects contribute to the hysteresis. At larger

*Corresponding author. Email: remi.delville@ua.ac.be

ISSN 1478–6435 print/ISSN 1478–6443 online

DOI: 10.1080/14786430903074755
http://www.informaworld.com

scales, interactions between domains, as well as heat transfer, play a role. Recent findings [1], however, suggest that interactions at interfaces between the martensitic and austenitic phases during phase transformation might be the dominant phenomenon contributing to hysteresis. This result is supported by the latest development in the geometric non-linear theory of martensite (GLNTM) [3,4], which explains the formation of martensite microstructures, the shape memory effect and the role of crystalline symmetry and phase compatibilities. This theory gives several conditions for SMAs to show extremely low hysteresis [1,3,5]. The first condition is no volume change during phase transformation, which, in mathematical terms, translates to $\det(U) = \lambda_1\lambda_2\lambda_3 = 1$, where U is the positive-definite, symmetric transformation matrix that maps the martensite lattice to the austenite lattice, $\det(U)$ is the determinant and $\lambda_1 \leq \lambda_2 \leq \lambda_3$ are the ordered eigenvalues of U. The second condition $\lambda_2 = 1$ is necessary and sufficient so that there is a perfect interface – unstressed and untwinned – between austenite and martensite. This is referred to in the text as phase compatibility. The six transformation matrices U_1–U_6 for the cubic (B2) to orthorhombic (B19) phase transformation are shown in Equation (1). Their values are entirely determined by the lattice parameters of the austenite (a_0) and martensite phases (a, b, c):

$$U_1 = \begin{pmatrix} \beta & 0 & 0 \\ 0 & \frac{\alpha-\gamma}{2} & \frac{\alpha+\gamma}{2} \\ 0 & \frac{\alpha+\gamma}{2} & \frac{\alpha-\gamma}{2} \end{pmatrix} \quad U_2 = \begin{pmatrix} \beta & 0 & 0 \\ 0 & \frac{\gamma-\alpha}{2} & \frac{\alpha+\gamma}{2} \\ 0 & \frac{\alpha+\gamma}{2} & \frac{\gamma-\alpha}{2} \end{pmatrix}$$

$$U_3 = \begin{pmatrix} \frac{\alpha-\gamma}{2} & 0 & \frac{\alpha+\gamma}{2} \\ 0 & \beta & 0 \\ \frac{\alpha+\gamma}{2} & 0 & \frac{\alpha-\gamma}{2} \end{pmatrix} \quad U_4 = \begin{pmatrix} \frac{\gamma-\alpha}{2} & 0 & \frac{\alpha+\gamma}{2} \\ 0 & \beta & 0 \\ \frac{\alpha+\gamma}{2} & 0 & \frac{\gamma-\alpha}{2} \end{pmatrix}$$

$$U_5 = \begin{pmatrix} \frac{\gamma-\alpha}{2} & \frac{\alpha+\gamma}{2} & 0 \\ \frac{\alpha+\gamma}{2} & \frac{\gamma-\alpha}{2} & 0 \\ 0 & 0 & \beta \end{pmatrix} \quad U_6 = \begin{pmatrix} \frac{\gamma-\alpha}{2} & \frac{\alpha+\gamma}{2} & 0 \\ \frac{\alpha+\gamma}{2} & \frac{\gamma-\alpha}{2} & 0 \\ 0 & 0 & \beta \end{pmatrix}$$

$$\beta = \lambda_1 = \frac{a}{a_0} \quad \alpha = \lambda_2 = \frac{b}{\sqrt{2}a_0} \quad \gamma = \lambda_3 = \frac{c}{\sqrt{2}a_0}. \tag{1}$$

When Cui et al. [1] investigated the dependence of hysteresis with these two parameters on composition-spread TiNiCu and TiNiPd thin-films, they discovered a strong correlation between hysteresis and λ_2, but not with $\det(U)$. The same correlation was confirmed by Zhang et al. [6] for bulk alloys of TiNiAu, TiNiPd and TiNiPt. Figure 1 shows the evolution of hysteresis as a function of λ_2 for the $Ti_{50}Ni_{50-x}Pd_x$ bulk alloys used for the present TEM investigation. The hysteresis decreases as λ_2 approaches 1 and is minimal when perfect compatibility is achieved ($Ti_{50}Ni_{40}Pd_{10}$ and $Ti_{50}Ni_{39}Pd_{11}$). These data were also reported in [6] except for the $Ti_{50}Ni_{40}Pd_{10}$ alloy. Similar plots were obtained for the TiNiAu, TiNiPt and TiNiCu systems in bulk or thin-film, as shown in [6].

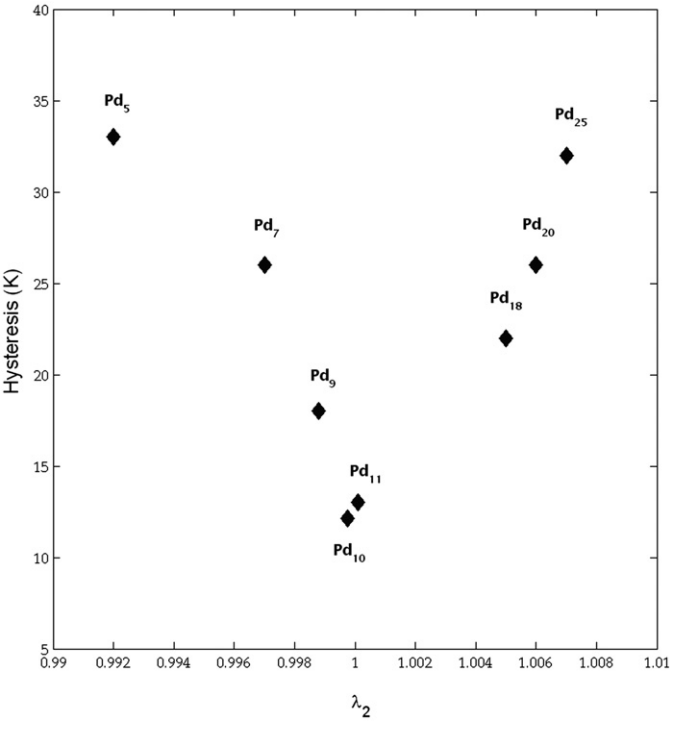

Figure 1. Width of hysteresis versus λ_2 for the $Ti_{50}Ni_{50-x}Pd_x$ bulk alloys system. The atomic percentage of Pd is indicated by Pd_x.

This finding underlines the importance of phase compatibility for hysteresis, which seems to follow a universal behavior as a function of λ_2. A typical interface between the austenitic phase and martensitic phase in an alloy with $\lambda_2 \neq 1$ is shown in Figure 2 [7,8]. Since a single variant of martensite is not compatible with the parent phase, the microstructure accommodates the interface with a laminate of two variants to minimize energy. The interface as seen in Figure 2 is neither sharp nor particularly well defined, and a large transition layer with tapering of twins is visible. One can already foresee from this picture that such an interface will induce some strain, especially in the twinned martensite. This was confirmed by Sun et al. [9,10] who used Moiré interferometry pattern at an austenite–martensite interface in CuAlNi and found a high number of fringes in the martensite, revealing a high level of strain. It also shows that on the scale allowed by the resolution of the technique, the deformation is homogenous with a constant deformation gradient. At the scale of atomic resolution transmission electron microscopy, techniques such as geometric phase analysis allow one to map strain fields around precipitates or at interfaces, as attempted by Hÿtch et al. [11] for a coherent microtwinned interface in Cu–Zn–Al.

The idea behind hysteresis is that the main energy barrier of the phase transformation arises from the bulk energy of this transition layer and the interfacial energy of the twin bands. The growth of a fully developed austenite–martensite interface is costly in energy but it can be greatly reduced by making martensite and

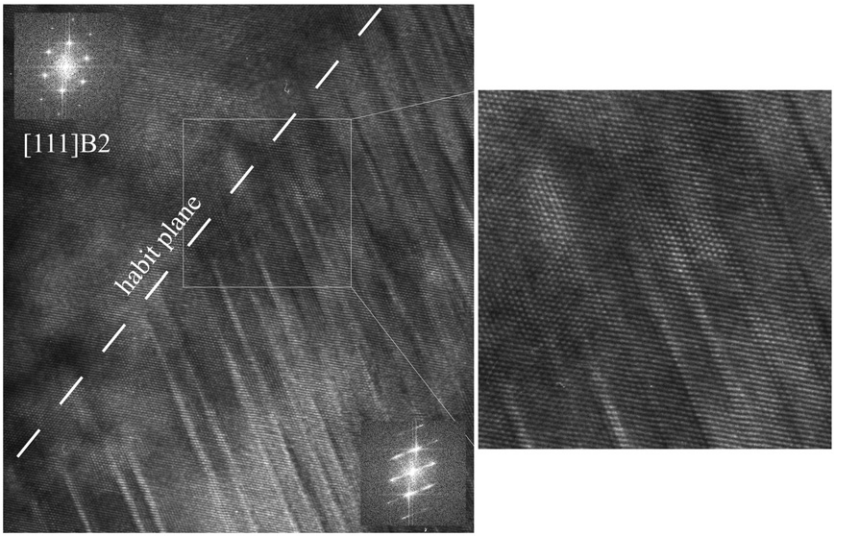

Figure 2. High resolution transmission electron micrograph of an austenite–martensite interface in splat-cooled $Ni_{62.5}Al_{37.5}$. The inset shows a magnification of the rectangular area revealing the atomic resolution near the interface.

austenite compatible. The study with electron microscopy of low hysteresis alloys near compatibility is, therefore, an important source of information to understand the impact of phase compatibility on the microstructure and how it relates to low hysteresis. The $Ti_{50}Ni_{50-x}Pd_x$ system was chosen because its composition can be tuned to achieve the condition $\lambda_2 = 1$, where it shows a very small hysteresis, and it can be easily prepared for TEM investigation.

2. Experimental

Alloys were prepared from pure elements (99.98 mass% Ti, 99.995 mass% Ni, 99.95 mass% Pd) by arc melting in an argon atmosphere. Slabs of 1 mm or less in thickness were cut from the ingot by EDM (electrical discharge machining) and subsequently homogenized at 1373 K for 20 ks followed by quenching in room-temperature water. Lattice parameters of both martensite and austenite were measured on a Scintag X-ray diffractometer on polycrystalline slabs, previously chemically etched using an electrolyte of 85% CH_3COOH and 15% $HClO_4$. Transformation temperatures and hysteresis were measured by differential scanning calorimetry (DSC) on a TA Instruments Q1000 with 100-μm thick slabs, previously etched by the same method. For the TEM study, disks of 3 mm in diameter were spark-cut or slurry-drilled from the slabs, mechanically polished to a 200-μm thickness and finally electropolished to perforation in a Tenupol 3 operated at 12 V, 0.1 A, 253 K with an electrolyte of 80% CH_3OH and 20% H_2SO_4. Conventional transmission electron microscopy (CTEM) observations were carried out in a Phillips CM20 microscope operated at 200 kV using a side-entry type double-tilt

Table 1. Lattice parameters of the austenite B2 phase (a_0) and the martensite B19 phase (a, b, c) in Ångstrom units. The middle eigenvalue λ_2 is equal to $b/(\sqrt{2}.a_0)$. It decreases as Pd decreases for the series studied. θ_c is defined as the average of the four characteristic transformation temperatures, $\theta_c = (A_s + A_f + M_s + M_f)/4$ and the hysteresis as $H = (A_s + A_f - M_s - M_f)/2$.

Alloys	a_0 (Å)	a (Å)	b (Å)	c (Å)	λ_2	θ_c (K)	H (K)
$Ti_{50}Ni_{43}Pd_7$	3.0318	2.8493	4.2747	4.5474	0.9970	−20	26
$Ti_{50}Ni_{41}Pd_9$	3.0469	2.8461	4.3036	4.5827	0.9988	40	18
$Ti_{50}Ni_{40}Pd_{10}$	3.0471	2.8436	4.3083	4.5934	0.9998	23	12
$Ti_{50}Ni_{39}Pd_{11}$	3.0499	2.8304	4.3135	4.6041	1.0001	25	13
$Ti_{50}Ni_{32}Pd_{18}$	3.0556	2.8194	4.3429	4.6281	1.0050	113	22
$Ti_{50}Ni_{30}Pd_{20}$	3.0508	2.8202	4.3404	4.6126	1.0060	103	26
$Ti_{50}Ni_{25}Pd_{25}$	3.0625	2.8074	4.3614	4.6667	1.0070	189	32

specimen holder with angular ranges of ±45°. High resolution electron microscopy (HREM) and CTEM observations were carried out in a FEG Phillips CM30 microscope operated at 300 kV using a side-entry type double-tilt specimen holder.

The $Ti_{50}Ni_{50-x}Pd_x$ system undergoes a martensitic transformation on cooling from a cubic (B2) to an orthorhombic (B19) lattice for compositions above $x = 7$ [12,13]. This transformation gives rise to six variants of martensite, denoted 1 to 6. Each of the possible transformations can be described by its own transformation strain matrix, U_1–U_6, as listed in Equation (1). Lattice parameters of austenite (a_0) and martensite (a, b, c), listed in Table 1 for the different compositions studied, were measured on a Scintag X-ray diffractometer outfitted with a temperature-controlled stage. Special attention was paid to alignment by using internal standard (NIST standard reference 640c) and periodically doing *in situ* alignment at different temperatures. The arc-melted, solution-treated alloys have an average grain size of 100 μm. A modified Rietveld procedure was used for refinement. The standard error on the determination of lattice parameters was estimated at $\pm 1 \times 10^{-3}$ Å. The middle eigenvalue λ_2 was directly calculated from the lattice parameters. The standard error on λ_2 is $\pm 5 \times 10^{-4}$. In addition, Table 2 shows the average value of the four characteristic transformation temperatures $\theta_c = (A_s + A_f + M_s + M_f)/4$ and the thermal hysteresis defined as the difference between the transformation temperatures of the austenitic and martensitic transformation, i.e. $H = A_s + A_f - M_s - M_f/2$.

Variants are associated in pairs to form twins. The pairs 1–2, 3–4, 5–6 have a compound twin connection and all other pairs (e.g. 1–3) have type I/type II twin connections. Table 2 shows the twin parameters for three selected alloys calculated with the GNLTM. K_1 is the twinning plane and η_1 the shear direction. There are three twinning modes, {111} type I, ⟨211⟩ type II and {011} compound. Only the values of the irrational planes and directions depend on the composition. It has been shown that, in the frame of the GNLTM [6,14], type I/II twins cannot participate in the austenite-martensite interface when $\lambda_2 < 1$, and conversely compound twins cannot participate when $\lambda_2 > 1$. For this reason the twin ratio λ, defined such that $\lambda/(1-\lambda)$ is the volume fraction of the smaller variant participating in the

Table 2. Twinning modes and twin ratios for $Ti_{50}Ni_{50-x}Pd_x$, $x = 9$, 11, 20, calculated from the GNLTM. K_1 is the twinning plane and η_1 the shear direction. The twin ratio is defined as the width ratio between two martensite variants accommodating a habit plane with the austenite.

Type of twins	x	K_1	η_1	Twin ratio λ	λ_2
{111} type I	9		⟨1 −0.21 −0.80⟩	ø	0.9988
	11	{111}	⟨1 −0.23 −0.77⟩	0.003	1.0001
	20		⟨1 −0.26 −0.74⟩	0.15	1.0060
⟨211⟩ type II	9	{0.59 −0.18 −1}		ø	0.9988
	11	{0.60 −0.20 −1}	⟨211⟩	0.004	1.0001
	20	{0.63 −0.26 −1}		0.18	1.0060
{011} compound	9			0.019	0.9988
	11	{011}	⟨01–1⟩	ø	1.0001
	20			ø	1.0060

austenite-martensite interface, only has meaning when these conditions are satisfied. The closer λ_2 is to 1, the smaller the twin ratio λ is.

3. Results and discussions

3.1. *Evolution of the microstructure*

Figures 3a–c shows the evolution of martensite morphology as the content of Pd is decreased towards the compatibility condition $\lambda_2 = 1$. The alloy with the highest Pd content, $Ti_{50}Ni_{25}Pd_{25}$, has a $\lambda_2 = 1.0070$, the largest value in the series studied. Its morphology (Figure 3a) is one commonly found in SMAs with long martensite plates made up of parallel planar layers of twinned martensite variants, sometimes referred to as twin laminates. The twin laminates extend diagonally across the width of the martensite plates with regular spacing. Their orientations alternate between configuration A and B in successive plates (Figure 3a). The same relative orientation between successive plates was found throughout the sample. Selected area diffraction (SAD) patterns in Figures 3d and e were taken from the twin laminates in plates A and B (Figure 3a) in two different orientations, the beam edge-on with the twinning plane. Each pattern consists of two sets of reflections which are in mirror symmetry with respect to the (111) plane. The same {111} type I twin is found throughout the sample and is considered to be the lattice invariant shear (LIS), which means that martensite is sheared along this mode to accommodate a habit plane with austenite during the phase transformation. The same morphology and LIS twinning of the laminates were reported for higher Pd content [15,16].

As the content of Pd decreases, so does λ_2. $Ti_{50}Ni_{30}Pd_{20}$ ($\lambda_2 = 1.0050$) shows some significant changes in its microstructure compared to higher Pd alloys. The lamellar morphology of the martensite plates is partly retained, but many plates now exhibit a lower twin ratio or even no twinning. Figure 3b is a bright-field micrograph of a martensite plate in $Ti_{50}Ni_{30}Pd_{20}$ showing a lower twin ratio than in $Ti_{50}Ni_{25}Pd_{25}$. In addition, the surrounding plates do not show any twinning. Overall, the

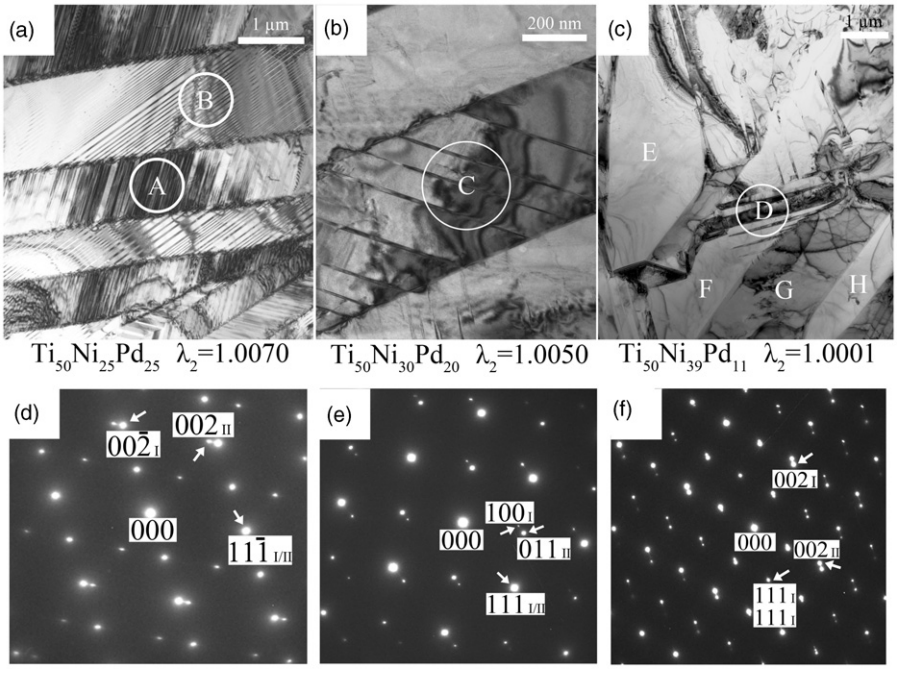

Figure 3. Evolution of microstructure with composition in bright-field images (a)–(c). (a) Internally twinned martensite plates in $Ti_{50}Ni_{25}Pd_{25}$. (b) Plate in $Ti_{50}Ni_{30}Pd_{20}$ with a smaller twin ratio. (c) Example of microstructure in $Ti_{50}Ni_{39}Pd_{11}$ composed of a mosaic of twinless martensite plates denoted E, F, G, H and a group of compound twins (D). SAD patterns (d,e) correspond to plates A and B in (a) showing {111} type I twins with the incident electron beam B//[1–10]I for (d) and B//[01–1]I for (e). SAD pattern (f) was taken over the circled area D and belongs to (011) compound twins observed in the [001] direction. The two variants are indexed I and II.

microstructure has a more disorganized morphology, a feature amplified in $Ti_{50}Ni_{39}Pd_{11}$.

$Ti_{50}Ni_{39}Pd_{11}$ has one of the lowest hysteresis from the series shown in Figure 3 and a $\lambda_2 = 1.0001$, meaning that virtually no lattice invariant shear is required for an undistorted plane (habit plane) to exist during transformation. This compatibility between a single variant of martensite and the austenite matrix allows for twinless transformation that minimizes the overall energy of interfaces, leading to a lower hysteresis. Figure 3c shows an example of microstructure commonly observed in $Ti_{50}Ni_{39}Pd_{11}$. It is composed of a mosaic of microns-wide twinless martensite plates, noted by E, F, G, H in Figure 3c. The absence of twin laminates inside the plates was also reported for $Ti_{79}Ta_{21}$ [17], $Ti_{49.5}Ni_{40.5}Cu_{10}$ [18,19] and $Ti_{50}Ni_{30}Cu_{20}$ [20], which also have a λ_2 close to 1.

{111} type I LIS twin laminates observed for the higher Pd content are a product from the accommodation of martensite at the interface with austenite during phase transformation. Plates of martensite will only grow as laminates of two variants since a single variant is not compatible with the austenite. However, when perfect compatibility is satisfied, as for Pd content around 11 at %, plates composed of a

single variant can develop. The resulting microstructure is determined by the local nucleation conditions and the ensuing growth of martensite plates. One process shaping the microstructure consists in the simultaneous growth of several monovariant plates from one nucleation site in a self-accommodated group of plates (SAG) morphology to minimize the transformation strain. SAGs are also observed in $\lambda_2 \neq 1$ alloys such as binary Ni–Ti [21,22]. In that case, the SAGs are composed of laminated martensite plates that accommodate an interface with austenite during growth. Typical triangular SAGs, as described by Saburi et al. [23] in TiNiCu, were observed in $Ti_{50}Ni_{39}Pd_{11}$ and reported in [24]. Another possible process shaping the microstructure may be the impinging of plates (or SAG) that have nucleated at different locations. For $Ni_{65}Al_{35}$ martensite, Boullay et al. [25] have shown that impinging laminar plates, not corresponding with orientations appearing in SAGs, undergo a small rotation to meet along an energy-minimizing interface. In the case of $\lambda_2 = 1$ alloys, single variants will impinge on each other and their interface may form a twin boundary after a small rotation. The twin type would then depend on the pair of variants under consideration. The three types of possible twins, namely {011} compound (Figure 3c), {111} type I and ⟨211⟩ type II (Figure 4a) were found in $Ti_{50}Ni_{39}Pd_{11}$. Figure 4a illustrates an area in $Ti_{50}Ni_{39}Pd_{11}$ which could have possibly been formed along the two mechanisms described above. The boundaries noted B and C are {111} type I twin and are formed by three variants in a triangular SAG in accordance with the model proposed by Saburi et al. [23]. A ⟨211⟩ type II interface was found in the interface denoted D and could have been created through the impingement of plates.

It has also been observed that the largest monovariant martensite plates are present in areas free of defects and precipitates where they were able to grow unconstrained. Areas with $Ti_2Ni(Pd)$ precipitates or defects contain smaller plates and a higher density of interfaces, since martensite had to accommodate local stress fields and since the number of nucleation sites is potentially higher.

It is worth mentioning that this special microstructure is not limited to $Ti_{50}Ni_{39}Pd_{11}$, it has also been observed in alloys with a slight difference in composition but with a λ_2 remaining close to 1 (roughly in the range $\lambda_2 = 1.000 \pm 0.004$) such as $Ti_{50}Ni_{41}Pd_9$ and in some parts of $Ti_{50}Ni_{32}Pd_{18}$ or even $Ti_{50}Ni_{30}Pd_{20}$. One has to be aware that the value of λ_2 is derived from X-ray measurements, which averages lattice parameters over the bulk. Local variations of composition appear in the bulk sample, hence local variations of lattice parameters are not to be excluded and could explain why certain types of twins appear in certain areas, whereas large twinless plates appear in others. In addition, certain samples contain a small quantity of $Ti_2Ni(Pd)$ precipitates, which locally alter the composition of the surrounding matrix, as confirmed by EDS measurements. However, compositional or lattice parameter variations within the matrix, away from precipitates could not be confirmed by EDS or EELS spectroscopy and LACBED, respectively. Also, since the averaged austenite grain size measured from X-ray diffraction as well as the size of the resulting martensite plates as observed in TEM does not show large variations between the different compositions, no grain nor plate size effect, as found in, e.g. Ni_xAl_{100-x} samples with different composition or thermomechanical history [26], is expected in the present case.

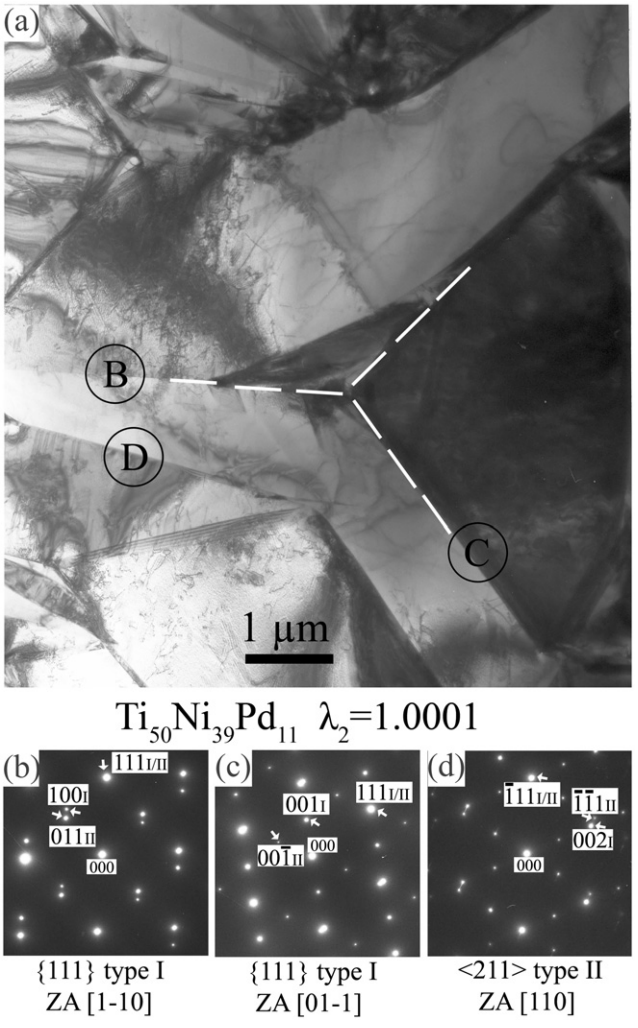

Figure 4. Example of microstructure in a compatible alloy $Ti_{50}Ni_{39}Pd_{11}$. The martensite plates exhibit no internal twin laminates. Some boundaries between plates in $Ti_{50}Ni_{39}Pd_{11}$ were found to be in twin orientation. (b)–(d) SAD patterns taken from the circled areas B, C, D, respectively. They show {111} type I twin (B, C) and a ⟨211⟩ type II twin (D). The zone axis (ZA) of the diffraction patterns are indicated on the figure.

3.2. *Austenite–martensite interface*

To gain further insight into the mechanism of transformation with phase compatibility, it is necessary to study the austenite (B2)/martensite (B19) interface. $Ti_{50}Ni_{40}Pd_{10}$ presents the proper conditions for such study. First of all, its transformation temperatures lie near room temperature, thus allowing the simultaneous observation of martensite, austenite and their common interfaces. Secondly, with a $\lambda_2 = 0.9998 \pm 0.0005$, $Ti_{50}Ni_{40}Pd_{10}$ satisfies exactly the compatibility condition within the error bar and shows the smallest hysteresis of the series, measured at 6 K

from the DSC curve presented in Figure 5. A sample of 6.2 mg was mounted on a differential scanning calorimeter (DSC Q2000-TA instruments). The sample was cycled twice between 220 and 370 K at a heating and cooling rate of 5 K/min. No difference was observed between the two cycles.

From the DSC graph (Figure 5), the temperatures of the peak-maxima related to the reverse (heating) and forward (cooling) transformation show a hysteresis of about 12 K. A heat-flow of about 16 J/g was calculated for both reverse and forward transformation.

The $Ti_{50}Ni_{40}Pd_{10}$ samples prepared for TEM were usually composed of an austenite matrix, within which a few plates of martensite had nucleated. It was, however, possible to increase the number and size of the martensite plates by cooling the sample before and during the thinning by electropolishing.

Figure 6a shows a typical arrangement of martensite plates embedded in an austenite matrix. The microstructure comprises two groups of parallel martensite lamellas noted A and B. Each group of plates forms interfaces with austenite along a common habit plane. This plane is rotated 90° between groups A and B. SAD patterns taken over the circled areas A and B in Figure 6a are shown in Figures 6b and e, respectively. Both show two sets of reflections. One belongs to the B2 matrix orientated in the [011] direction and the other to the B19 phase in a [010] zone axis. The common $[010]_{B19}$ zone axis entails that the groups of martensite plates in area A and B belong to the same variant since no variants in the cubic to orthorhombic phase transformation share a common [010] axis. The sets of B2 reflections (red online in Figures 6d and g) coming from the austenite matrix share the same position in both patterns. The set of B19 reflections (black in Figures 6d and g) is slightly rotated clockwise in area A and counter-clockwise in area B, relative to the B2 set. To understand this observation, a simulation of the interfaces has been carried out.

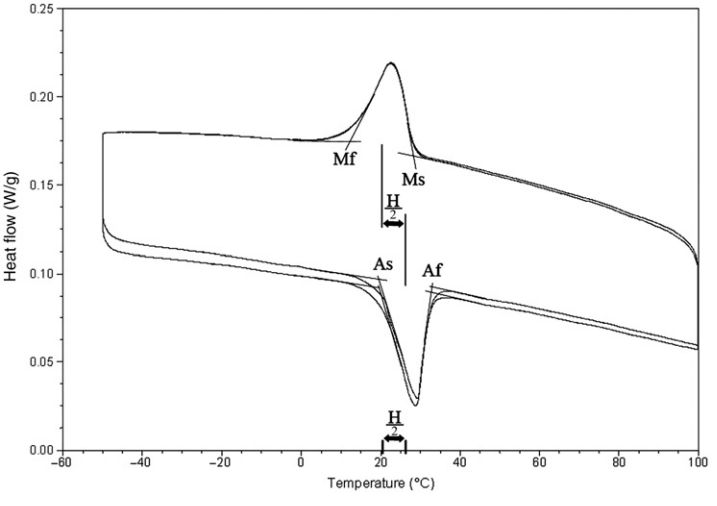

Figure 5. DSC curves of $Ti_{50}Ni_{40}Pd_{10}$. The cubic to orthorhombic phase transformation exhibits a very small hysteresis measured as $H = A_s + A_f - M_s - M_f/2$.

Firstly, the possible habit planes are calculated from the fundamental compatibility equation of the GNLTM (Equation (2)):

$$QU_i - I = a \otimes n, \tag{2}$$

where U_i is the transformation matrix of variant i ($i = 1, \ldots, 6$); I is the identity matrix representing the austenite, Q is a rotation matrix, a is the direction of shear and n is the normal vector of the habit plane. The results for all variants are given in Table 3.

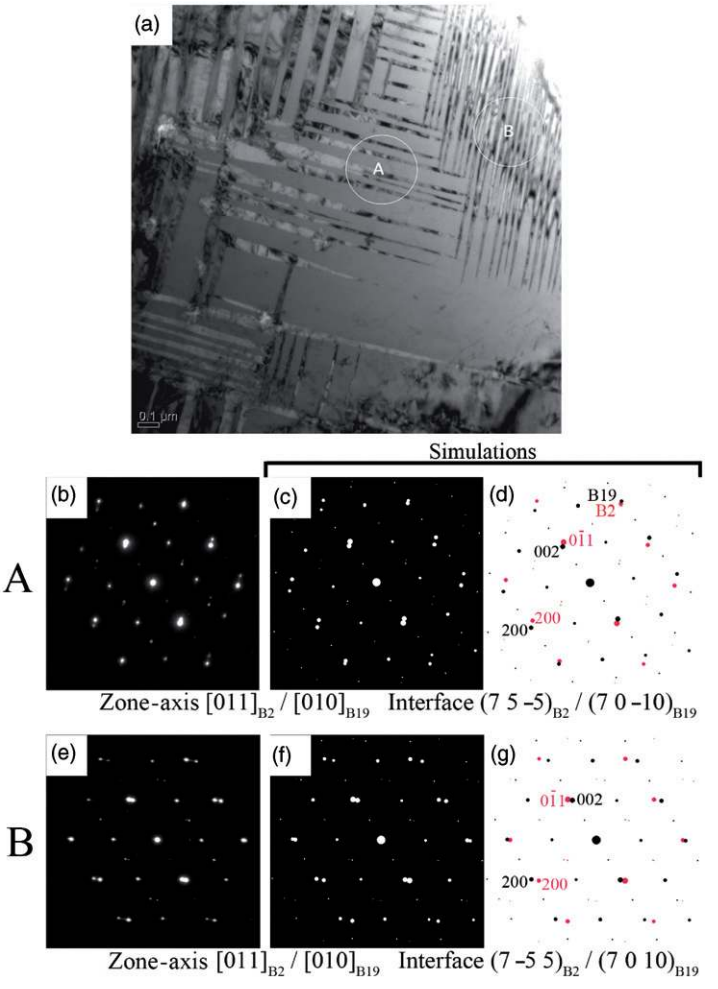

Figure 6. (Color online). Microstructure and crystallography of $Ti_{50}Ni_{40}Pd_{10}$. (a) Bright-field micrograph showing plates of martensite aligned along the two perpendicular directions of habit planes inside an austenite matrix. (b) and (e) SAD patterns taken over the two circled areas A and B and the corresponding simulations using parameters derived from the GNLTM. Both series show two sets of reflections corresponding to the $[011]_{B2}/[010]_{B19}$ zone-axis patterns. The B19 set of reflections is slightly rotated relative to the B2 set, with an opposite angle for the A and B areas.

Table 3. Calculated habit planes for the six variants of martensite ($U_1 - U_6$). The results are given in the austenite (B2) and martensite (B19) basis. Irrational plane indices are approximated to the closest set of integers.

	Habit plane 1		Habit plane 2	
	B2 basis	B19 basis	B2 basis	B19 basis
U_1	(7−5 5)	(7 0 10)	(7 5−5)	(7 0−10)
U_2	(−7 5 5)		(7 5 5)	
U_3	(5 7−5)		(−5 7 5)	
U_4	(5−7 5)		(5 7 5)	
U_5	(−5 5 7)		(5−5 7)	
U_6	(5 5−7)		(5 5 7)	

Each variant gives two habit plane solutions. The following calculations will be done by fixing one of the variants as variant 1. It can be shown that all other cases are symmetrically related to this one. Habit planes calculated for variant 1 are (7−5 5) and (7 5−5) in the cubic basis, (7 0 10) and (7 0−10) in the martensite basis. Figure 7 is a stereographic projection in the $[011]_{B2}/[010]_{B19}$ direction showing traces of the calculated habit planes. The projection was orientated using the diffraction pattern of the B2 matrix. Traces of $(7-5\ 5)_{B2}$ and $(7\ 5-5)_{B2}$ (red lines) planes are consistent with the habit planes directions observed in the bright-field picture (Figure 6a). Traces of $(7\ 0\ 10)_{B19}$ and $(7\ 0-10)_{B19}$ planes were positioned on the projection using the lattice correspondences between the austenite and variant 1, i.e. without rotation. It then becomes obvious from the projection that there is a few degrees mismatch around the $[011]_{B2}$ axis between the pairs of planes $(7-5\ 5)_{B2}/(7\ 0\ 10)_{B19}$ and $(7\ 5-5)_{B2}/(7\ 0-10)_{B19}$. This is accommodated by a rotation of the martensite as shown by the black arrows in Figure 7. The direction of rotation depends on which habit plane is accommodated and explains the difference in the position of the set of B19 reflections observed in the diffraction pattern in area A ($(7\ 5-5)_{B2}$ habit plane) and B ($(7-5\ 5)_{B2}$ habit plane) in Figures 6b,e and 8b,c. A representation of lattice correspondences and the rotation direction is presented Figure 8a. One can compute the precise angle of rotation by extracting it from the rotation matrix given by Equation (3):

$$Q = (a \otimes n + I)U_i^{-1}. \tag{3}$$

The rotation matrix Q gives the axis of rotation Γ and the angle of rotation α listed in Table 4. As shown in Figure 8, the experimental rotation is in good agreement with the calculated one.

As mentioned before, there are strong indications that the interfacial energy between austenite and martensite contributes strongly to the hysteresis. Consequently, low-hysteresis SMAs are believed to have low energy B2/B19 boundaries. To sustain this assertion, a high resolution study of this interface was attempted. One of the conditions to obtain interpretable high resolution images of the interface is to observe it edge-on along a direction where both phases are in zone

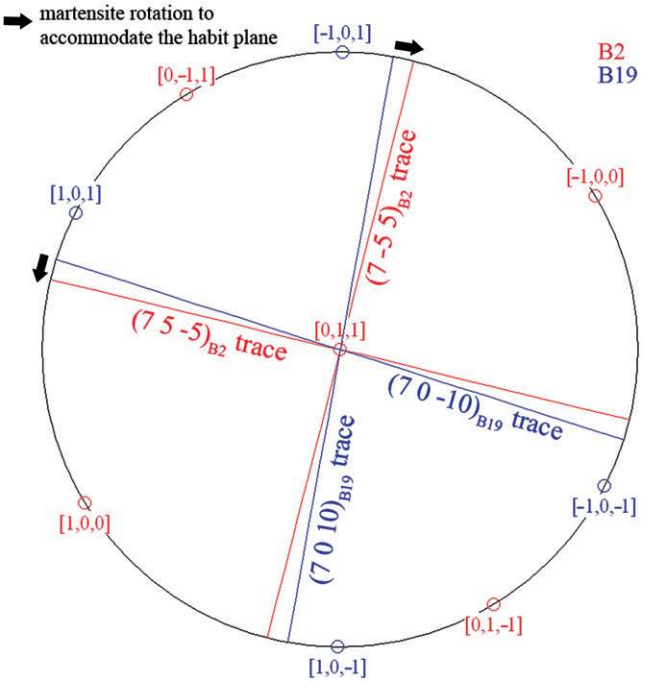

Figure 7. (Color online). Trace analysis of habit planes in $Ti_{50}Ni_{40}Pd_{10}$. The traces of the two calculated habit planes for variant 1 are drawn for the B2 (red) and B19 (blue) phases in the $[011]_{B2}/[010]_{B19}$ directions, before rotation of the martensite, using only lattice correspondences. The B2 traces directions are consistent with the habit planes directions observed in Figure 6a. A small angle misfit is observed between the $(7\ 5-5)_{B2}/(7\ 0-10)_{B19}$ and the $(7-5\ 5)_{B2}/(7\ 0\ 10)_{B19}$ planes traces. This is accommodated by a rotation of the martensite, as shown by the black arrows.

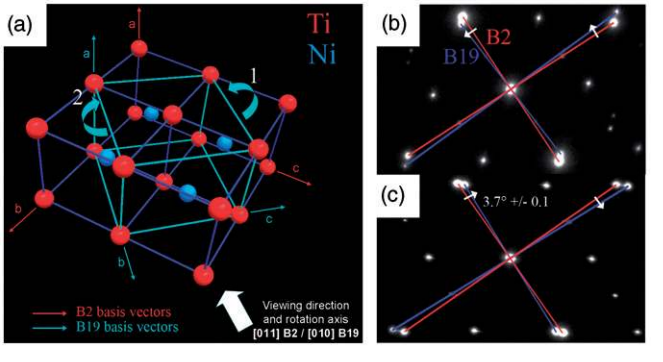

Figure 8. (Color online). Lattice correspondences and martensite rotation. (a) 3D representation of lattice correspondences for variant 1. The white arrow represents the observation axis of Figure 6a. Depending on the habit plane, the martensite rotates in the '1' or '2' directions. The rotation axis is $[011]_{B2}$. (b) and (c) Enlargements of the diffraction patterns from area A and B in Figures 6b and e. The blue lines show how the set of B19 reflections was rotated in the '1' direction (b) or '2' direction (c) relative to the set of B2 reflections (red lines). The rotation angle is measured at $3.7 \pm 0.1^{\circ}$, in good agreement with the calculated value of 3.8°.

Table 4. Angle and axis of rotation extracted from the rotation matrix Q for the two habit planes solutions for the six variants.

Variant	Habit plane	Angle α	Rotation axis Γ
U_1	(7 −5 5) (7 5 −5)	−3.8° 3.8°	[011]
U_2	(−7 5 5) (7 5 5)	−3.8° 3.8°	[01 −1]
U_3	(5 7 −5) (−5 7 5)	−3.8° 3.8°	[101]
U_4	(5 −7 5) (5 7 5)	−3.8° 3.8°	[10 −1]
U_5	(−5 −5 7) (5 −5 7)	−3.8° 3.8°	[110]
U_6	(5 5 −7) (5 5 7)	−3.8° 3.8°	[1 −10]

orientation along a simple crystallographic axis. This condition is only met along the $[011]_{B2}/[010]_{B19}$ direction owing to the rotation of the martensite around this axis. In addition to this restrictive condition, another experimental difficulty comes from the sensitivity of the interface to beam heating. Under a prolongated exposure to a focused beam, the habit plane moves, the martensite being transformed into austenite.

Figure 9 shows a high resolution micrograph of an interface between a single variant of martensite and austenite in $Ti_{50}Ni_{40}Pd_{10}$ (or 'exact austenite-martensite interface'). The slightly rotated ($<4°$) $(001)_{B19}$ crystallographic planes (upper part) join the $(01-1)_{B2}$ planes (lower part) at the interface (habit plane) orientated along the $(75-5)_{B19}$ plane. When calculating the geometrical lattice spacing mismatch between the B2 and B19 projected along the trace of this plane, one finds only a small mismatch of 0.36%. In other words, the lattice planes join seamlessly at the interface with very little distortion, and no misfit defects were detected. This observation indicates a low energy boundary configuration.

The image simulation added to Figure 9 was performed using the multislice method implemented in MacTempas. The orientation relationship between the two superimposed lattices used for the simulation was taken from the GNLTM calculations. A more thorough simulation of the interface would require a DFT calculation of atomic positions near the interface. This would, in addition, provide a value for the interfacial energy. However, since the habit plane is irrational, periodic DFT cannot be directly implemented and a calculation would require a large supercell and/or an approximation of the habit plane as a rational plane. A quantitative estimation of interfacial energy could also be derived from a HREM image. It would require higher point resolution (0.17 nm for this microscope) supported by trough-focus reconstruction and/or aberration corrected microscopy to resolve atomic columns along the (01 – 1) B2 planes (d-spacing = 0.15 nm) and to quantify atomic displacements at the interface. Due to this limitation, it is also difficult to conclude if the interface is atomically sharp. If there is a transition layer

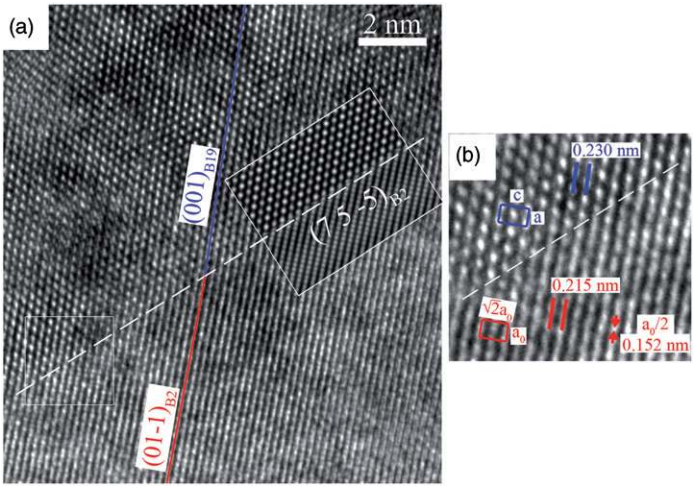

Figure 9. (Color online). HREM picture of an exact austenite–martensite interface. The upper part is the B19 phase in [010] orientation, the lower part is the B2 phase in [011] orientation. A simulation of the interface and the trace of the habit plane are added to the picture. The $(001)_{B19}$ (blue line) and $(01-1)_{B2}$ (red line) planes join seamlessly at the interface despite the small rotation of the martensite and a misfit of the lattices along the habit plane spacing as indicated in the enlargement of the inset.

with atomic displacements, it will not exceed a few angstroms, leading therefore to small interface energy, especially when compared to a classic habit plane as the one observed in the example of Ni–Al (Figure 2).

3.3. *Retained austenite in martensite near compatibility*

Several B2/B19 interfaces were also identified in the $Ti_{50}Ni_{30}Pd_{20}$, $Ti_{50}Ni_{32}Pd_{18}$ and $Ti_{50}Ni_{39}Pd_{11}$ samples. In contrast to the previous case, where interfaces were formed by martensite plates retained inside an austenite matrix, the present interfaces originate from very fine parallel lines of retained austenite (a few nanometers wide) embedded in a martensite matrix. Figure 10a is a bright-field image showing several of these lines inside a martensite plate. To elucidate their nature, SAED electron diffraction was performed. Figure 10b shows the resulting diffraction pattern. It shows two sets of reflections. The brighter spots belong to the B19 phase in [121] zone axis and the weaker spots originate from the line seen in bright-field and belong to the B2 phase in [131] orientation. The relative position of the two set of reflections fits with the model of B2/B19 habit plane presented previously, as shown in the simulated diffraction in Figure 10c. The presence of lines of retained austenite oriented along the habit plane for samples close to $\lambda_2 = 1$ can be explained by the fact that the austenite/martensite transition layer energy must be very small due to their compatibility. The observed austenite regions are a remnant of an incomplete transformation. It is also possible that a small scale fluctuation in composition resulted in a region with λ_2 closer to 1, or that the observed λ_2 was sufficiently close to 1 that a single interface transformation, accompanied by a delocalized elastic field, is preferred over a twinned austenite–martensite interface.

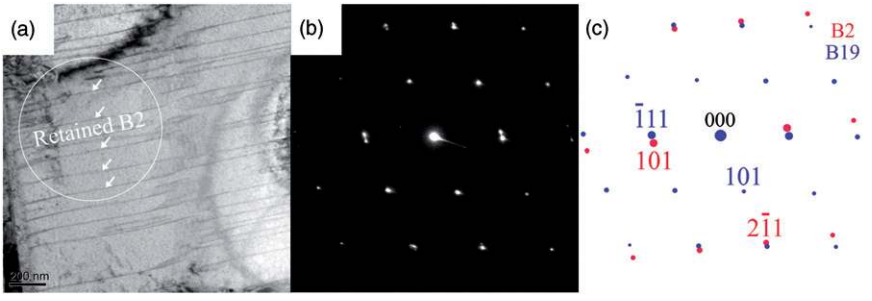

Figure 10. (Color online). (a) Bright-field image showing lines of retained austenite in $Ti_{50}Ni_{30}Pd_{20}$. The diffraction pattern in (b) shows two sets of reflections. One comes from the beam diffracted by the martensite in [121] zone axis and the other from retained austenite in [131] zone axis. (c) Simulated diffraction pattern using the habit plane parameters given by the GNLTM. The blue and red sets of reflections correspond to the B19 martensite and B2 austenite, respectively.

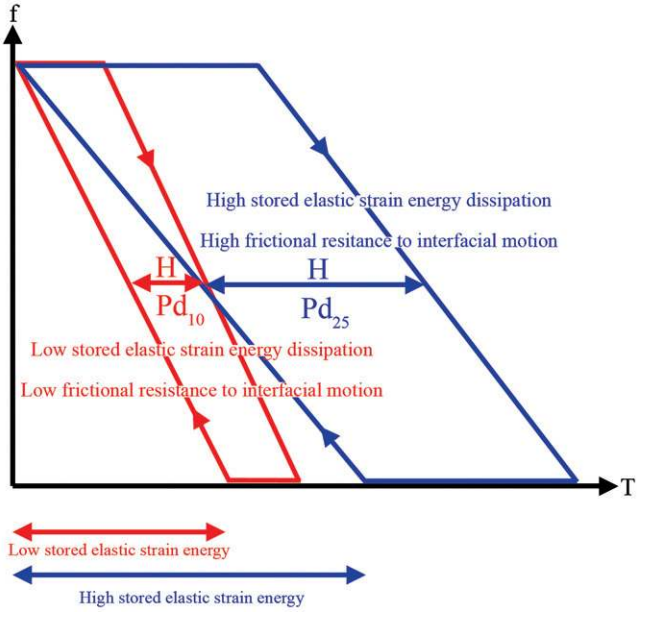

Figure 11. (Color online). Martensite volume fraction f versus temperature for the $Ti_{50}Ni_{25}Pd_{25}$ and $Ti_{50}Ni_{40}Pd_{10}$ alloys illustrating the contribution to the hysteresis loop. The slope of the curve is attributed to the stored elastic energy, which is recoverable, and the width of the loop is due to energy dissipation, which constitutes the hysteresis.

3.4. *Further discussion on hysteresis*

In a thermoelastic SMA, the non-chemical part of the energy transmitted to the system during the forward transformation (austenite to martensite) is stored as elastic strain within the martensite microstructure. In a perfectly reversible alloy, this elastic energy can be fully recovered upon reverse transformation. Dissipations mechanisms, however, occur and contribute to the hysteresis. Figure 11 shows the

martensite volume fraction evolution of the $Ti_{50}Ni_{25}Pd_{25}$ and $Ti_{50}Ni_{40}Pd_{10}$ samples with temperature (where M_f was set to 0 for both alloys for easier comparison) to illustrate the evolution of hysteresis. The slopes of the curves can be attributed to stored elastic energy. It is larger for $Ti_{50}Ni_{25}Pd_{25}$ due to the additional interface energy of the LIS laminates and higher misfit at interface between laminated plates when compared to the $Ti_{50}Ni_{40}Pd_{10}$ microstructure composed of monovariant plates.

The transformation loops show, however, a certain width (hysteresis) which is due to energy dissipation. Hamilton et al. [27] explain this irreversible component of the energy with two dissipative mechanisms. One is the frictional work spent overcoming the resistance to interfacial motion and the second is due to the dissipation of the stored elastic strain through relaxation of the coherency strains of the martensite–austenite interface. They observed the latter process in TEM with dislocations emitting from a martensite–austenite interface in a Ni–Ti single crystal. Their role is to reduce the remaining internal stress of the martensite variants at the habit plane. These dislocations accumulate over cycling and represent an additional frictional resistance to the habit plane motion. These irreversible processes, which are responsible for the hysteresis, are greatly reduced when $\lambda_2 = 1$, and explain the lower hysteresis observed for $Ti_{50}Ni_{40}Pd_{10}$ in Figure 11.

4. Conclusion

In studying the detailed nature of phase compatibility in the $Ti_{50}Ni_{50-x}Pd_x$ system, four aspects were considered: (a) the evolution of microstructure as phase compatibility is increased; (b) the crystallography of interfaces when one variant of martensite is compatible with the austenite; (c) the atomic arrangement at the interface using HREM; (d) the consequences of these results on the hysteresis.

The drop in hysteresis experienced by shape memory alloys when approaching the compatibility condition $\lambda_2 = 1$ is accompanied with important changes in the microstructure. For alloys with a $\lambda_2 \geq 1.005$, a typical laminar martensite morphology is observed. It is characterized by elongated plates of martensite composed of a laminate of two martensite variants. The plates also tend to organize themselves as laminates on a higher scale or occasionally along a more complicated self-accommodating pattern. When the compatibility condition is approached, one variant from the laminate becomes dominant until the plate becomes a single variant. The microstructure of $Ti_{50}Ni_{39}Pd_{11}$, which satisfies the compatibility condition, is characterized by the absence of laminates inside the martensite plates and by a complex arrangement of the plates resulting from their self-accommodation and impingement.

The crystallography of the interface between compatible B2 and B19 lattices in $Ti_{50}Ni_{40}Pd_{10}$ follow the predictions of the GNLTM. Each variant of martensite grows along two perpendicular habit planes after having rotated in a direction which depends on the selected habit plane.

The high resolution picture of the interface shows that atomic planes join seamlessly at the interface without misfit defects. The B2 and B19 lattices are barely disturbed and no significant transition layer with a strained lattice

could be identified. These observations suggest a low energy boundary configuration. In addition, the same alloy shows an extremely low hysteresis.

The low hysteresis observed in alloys satisfying the compatibility condition can be explained by a low dissipation of the elastic energy during transformation. Thanks to a good crystallographic fit between the two phases, the stress field is minimized and relaxation mechanisms, such as the generation of dislocations, are reduced.

Acknowledgements

The authors would like to thank MULTIMAT 'Multi-scale modeling and characterization for phase transformations in advanced materials', a Marie Curie Research Training Network (MRTN-CT-2004-505226) and the FWO project G.0465.05 'The functional properties of shape memory alloys: a fundamental approach' for supporting this work.

References

[1] J. Cui, Y.S. Chu, O.O. Famodu, Y. Furuya, J. Hattrick-Simpers, R.D. James, A. Ludwig, S. Thienhaus, M. Wuttig, Z. Zhang and I. Takeuchi, Nat. Mater. 5 (2006) p.286.
[2] J. Ortin and L. Delaey, Int. J. Non-Linear Mech. 37 (2002) p.1275.
[3] J.M. Ball and R.D. James, Phil. Trans. R. Soc. Lond. A. 338 (1992) p.389.
[4] J.M. Ball and R.D. James, Arch. Ration. Mech. Anal. 100 (1987) p.13.
[5] R.D. James and Z. Zhang, in *Magnetism and Structure in Functional Materials*, Vol. 79, L. Mañosa, A. Planes and A. Saxena eds., Springer Series in Materials Science, Springer, New York, 2005.
[6] Z. Zhang, S. Müller and R.D. James, Acta Mater. (2009) submitted.
[7] D. Schryvers, M. Yandouzi, D. Holland-Moritz and L. Toth, J. Phys. IV. 7 (1997) p.C5–203.
[8] D. Schryvers and D. Holland-Moritz, Intermetallics. 6 (1998) p.427.
[9] K. Bhattacharya, *Microstructure of Martensite*, Oxford University Press, 2003.
[10] Q.P. Sun, T.T. Xu and X. Zhang, J. Eng. Mater. Tech. 121 (1999) p.38.
[11] M.J. Hÿtch, Ph. Vermaut, J. Malarria and R. Portier, Mater. Sci. Eng. A. 273/275 (1999) p.266.
[12] V.P. Sivokha, A.S. Savvinov Voronin and V.N. Khachin, Phys. Met. Metall. 56 (1983) p.112.
[13] Y.C. Lo and S.K. Wu, Scripta Metall. Mater. 27 (1992) p.1097.
[14] K.F. Hane and T.W. Shield, J. Elast. 59 (2000) p.267.
[15] P.G. Lindquist, PhD thesis, University of Illinois at Urbana-Champaign, 1988.
[16] M. Nishida, T. Hara, Y. Morizono, A. Ikeya, H. Kijima and A. Chiba, Acta Mater. 45 (1997) p.4847.
[17] K.A. Bywater and J.W. Christian, Phil. Mag. 25/26 (1972) p.1249.
[18] T. Tadaki and C.M. Wayman, Metallography 15 (1982) p.247.
[19] T. Saburi, T. Komatsu, S. Nenno and Y. Watanabe, J. Less-Common Metals 118 (1986) p.217.
[20] W.J. Moberly, J.L. Proft, T.W. Duerig and R. Sinclair, Mater. Sci. Forum 56/58 (1990) p.605.
[21] K. Madangopal, Acta Mater. 45 (1997) p.5347.
[22] S. Miyazaki, K. Otsuka and C.M. Wayman, Acta Metall. 37 (1989) p.1873.

[23] T. Saburi, Y. Watanabe and S. Nenno, ISIJ Int. 29 (1989) p.405.
[24] R. Delville, D. Schryvers, Z. Zhang and R.D. James, Scripta Mater. 6 (2009) p.293.
[25] Ph. Boullay, D. Schryvers and J.M. Ball, Acta Mater. 51 (2002) p.1421.
[26] D. Schryvers, Phil. Mag. A. 68 (1993) p.1017.
[27] R.F. Hamilton, H. Sehitoglu, Y. Chumlyakov and H.J. Maier, Acta Mater. 52 (2004) p.3383.